Automatic landslide detection using Dempster–Shafer theory from LiDAR-derived data and orthophotos

Mustafa Ridha Mezaal, Biswajeet Pradhan, Helmi Zulhaidi Mohd Shafri & Zainuddin Md Yusoff

Taylor & Francis
Taylor & Francis Group

Automatic landslide detection using Dempster–Shafer theory from LiDAR-derived data and orthophotos

Mustafa Ridha Mezaal[a], Biswajeet Pradhan [a,b,c], Helmi Zulhaidi Mohd Shafri[a] and Zainuddin Md Yusoff[a]

[a]Department of Civil Engineering, Faculty of Engineering, Universiti Putra Malaysia, Selangor, Malaysia; [b]Faculty of Engineering and Information Technology, School of Systems, Management and Leadership, University of Technology Sydney, Ultimo, Australia; [c]Department of Energy and Mineral Resources Engineering, Sejong University, Seoul, Republic of Korea

ABSTRACT

A good landslide inventory map is a prerequisite for landslide hazard and risk analysis. In tropical countries, such as Malaysia, preparation of the landslide inventory is a challenging task because of the rapid growth of vegetation. Thus, it is crucial to use rapid and accurate technique and effective parameters. For this purpose, Dempster Shafer theory (DST) was applied in fusing high resolution LiDAR derived data products and Greenness index derived from orthophoto imagery. Two sites were selected, for the implementation and evaluation of the DST model; site "A" for DST implementation and site "B" for the comparison. For model implementation, vegetation index, slope and height were used as effective parameters for identifying automatic landslide detection. Two type of DST based fusions were evaluated; (greenness and height) and (greenness and slope). Furthermore, validation techniques were used to validate the accuracy are confusion matrix and area under the curve. The overall accuracy of the first and second evaluated fusions were (73.4% and 84.33%), and area under the curve were (0.76 and 0.81) respectively. Additionally, the result was compared with Random Forest (RF) based detection approach. The results showed that DST does not require a priori knowledge.

1. Introduction

Landslide is among the most destructive natural disasters worldwide, causing serious damages to lives and properties. It is triggered by other natural disasters, such as earthquakes and heavy rainfall that made it difficult to predict the landslides (Tehrany et al. 2014). Landslide inventory maps are required for various purposes such as: (1) recording the magnitude of landslide in a region, (2) performing the initial steps in analysing the susceptibility, hazard, and risk of the landslide (Van Westen et al. 2008; Guzzetti et al. 2012; Althuwaynee et al. 2014; Pradhan et al. 2016), and (3) examining the patterns of landslide distributions and studying the evolution of landscape affected by landslides (Parker et al. 2011; Pradhan et al. 2016). Producing a landslide inventory map is a challenging task due to rapid vegetation growth in tropical regions. It is difficult to detect the landslide location using the most available recognition techniques due to the covering effect of the vegetation. Thus, a rapid and accurate technique is required.

CONTACT Biswajeet Pradhan ✉ biswajeet24@gmail.com, biswajeet@lycos.com

Traditional techniques for producing landslide inventory maps are based on visual interpretation of aerial photographs. This interpretation needs several field surveys which is often time-consuming and expensive. However, one of the main disadvantages of the field mapping is that it is difficult to make a complete observation of big-scale landslides in certain areas especially in dense vegetated areas. Sometimes, it is difficult to visualize the old landslides using aerial photographs or satellite images due to the vegetation cover or the alteration caused by other slope failures and human activities (Miller et al. 2012). Consequently, this method enables the researchers to map and recognize single and small groups of landslides (Galli et al. 2008).

Optical and synthetic aperture radar (SAR) remote sensing has produced efficient progress in landslide inventory mapping. These data are useful in landslide studies that include, radar image (SAR), high spatial resolution multispectral image and digital elevation models (DEMs) obtained from spaceborne sensors and airborne laser scanning systems (Guzzetti et al. 2005; Ardizzone et al. 2007; Stumpf and Kerle 2011; Jebur et al. 2014). However, the accuracy of landslide detection using the above-mentioned data is affected by many factors: (1) dense vegetation that obscures the landslide (Wills and McCrink 2002; McKean and Roering 2004); (2) data interpretation which relies on the analysts' experience and their familiarity with the study area (Malamud et al. 2004; Chen et al. 2014); and (3) finally, the additional errors which can be introduced during translating the results of image interpretation to thematic maps (Malamud et al. 2004).

In general, LiDAR data has effective advantage over other remote sensing data because of its ability to penetrate densely vegetated areas by useful information of a terrain with a high point density (Mezaal et al. 2017; Pradhan and Mezaal 2017). High-resolution LiDAR-derived DEM depicts ground surface and provides useful information on topographic features where it is difficult to identify landslides covered under dense vegetation (McKean and Roering 2004). In a paper, Liu et al. (2012) used LiDAR-derived parameters (DTM (digital terrain model), DSM (digital surface model), height, etc.) and greenness index from orthophoto for automatic detection of landslide and achieved reasonable accuracy. Consequently, it is possible to fuse LiDAR-derived data together with high-resolution image data to delineate and identify surface feature; this process is called pan-sharpening or multi-sensory fusion (Vaiopoulos and Karantzalos 2016).

Fusion technique indicates extraction of information from two or more images by combining the information from these images. The output will be a readily high-performance single image data (Zhang and Blum 1997; Kaur et al. 2016) and has valuable information compared to unfused images (Pradhan et al. 2016). In recent years, a number of methods have been presented on different types of image fusion (Tu et al. 2004; Chu and Zhu 2008; Vu et al. 2009; Elghazali 2011; Gibril et al. 2016). However, several fusion techniques were developed and used to integrate data from different sensors (Yu et al. 2011). Elghazali (2011) used the Brovey transformation technique to fuse Quick-Bird image and LiDAR data for 2-D/3-D city mapping. Intensity–hue–saturation (IHS) transform-based fusion (Tu et al. 2004) and principal component analysis (PCA)-based fusion have also been applied in the literature (González-Audicana et al. 2004). Consequently, many studies have been developed for the optimization of various satellite imageries (Rottensteiner et al. 2005; Demir et al. 2009; Hnatushenko and Vasyliev 2016). In a recent paper, Pradhan et al. (2016) applied the wavelet transform technique to fuse LiDAR data and QuickBird image for automatic landslide detection.

Practically, all the above-mentioned fusion techniques provided an appreciable level of feature identification and extraction. Nevertheless, these techniques were limited by spectral degradation, especially when the data were acquired at different time points. This makes the results poorer than what is expected (Pradhan et al. 2016). Data elimination in some stages constitutes another factor that limits the use of full potential of the data sets. Likewise, the optimal use of these techniques is hampered by the number of bands as well as the number of sensor data (Mezaal et al. 2017). Furthermore, the difficulty of the mathematical explanations for readers constituted another limitation for determining the important theory behind wavelet-based fusion (Pradhan et al. 2016). The most popular image fusion techniques are IHS transform-based fusion, PCA-based fusion and Brovey transform

techniques. They are limited by three band combinations only. In this situation, LiDAR data derivatives, such as DTM, DSM, surface roughness and slope, cannot be fully exploited (Saeidi et al. 2014).

These limitations urged toward using an approach to fuse as many data as possible from different sensors (Mezaal et al. 2017). The data fusion technique, such as data Dempster–Shafer theory (DST) has been highlighted in many researches (Rottensteiner et al. 2005). Furthermore, the DST model has been successfully applied in many studies, such as geothermal potential mapping (Carranza et al. 2008), landslide susceptibility mapping (Althuwaynee et al. 2012; Bui et al. 2012; Mohammady et al. 2012; Feizizadeh and Blaschke 2013; Feizizadeh et al. 2014; Pradhan et al. 2014), groundwater potential mapping (Nampak et al. 2014), groundwater assessment (Feizizadeh et al. 2014), and groundwater pollution risk assessment (Neshat and Pradhan 2015).

DST considers every class and union of the classes to estimate probability mass functions to provide an efficient way of feature extraction from multi-sensor data (Bellenger and Gatepaille 2011). Moreover, it uses reasoning, weight, and probability-driven evidences in the data set. It is a pixel-based classifier that depends on the derivatives of sensor data set instead of the raw data (Hall and Llinas 1997). Handling of incomplete data and the associated degree of uncertainty makes DST a robust technique to exploit data from many sensors in a processing train (Rottensteiner et al. 2005). Reasoning-based system (Jiang et al. 2011) and empirical determination of parameters in DST make the concept generally applicable without depending on the satellite image (Rottensteiner et al. 2005). Furthermore, it is a time and cost-effective option as it reduces the period of time to select training sites (Kabolizade et al. 2010).

The main aim of this study is to implement DST by fusing LiDAR-derived data and greenness index derived from orthophoto imagery to identify the location of landslides. In addition, two sites were selected for the evaluations of the model: site 'A' for DST implementation and site 'B' for the comparison. The performance of evaluations fusion was validated to know which one is most appropriate for landslide detection. Finally, the comparison was conducted between the most appropriate evaluation and a recently published method based on random forest (RF) model.

2. Study area and datasets

The Cameron Highlands was chosen for the application of landslide detection because of the frequent occurrence of landslides. The study area covers an area of 26.7 km^2 and is located near the northern central part of Peninsular Malaysia (Figure 1). It is a tropical rainforest area characterized by dense vegetation cover and steep adjoining mountains. Geographically, Cameron Highlands is located in the zone of 4°24′32″–4°24′43″ latitudes and 101°22′54″–101°23′11″ longitudes in Malaysia. The altitude of the road is 1391 m above the mean sea level; meanwhile, the top of Cameron Highlands reaches 1540 m above mean sea level. The annual average rainfall is about 2660 mm, whereas the average daytime temperature of the area is moderate (∼24 °C) and at night-time reading 14 °C. A large part of the area (80%) is forested and the landform of the area ranges from flat terrain (0 degrees) to hilly area (80 degrees).

Two sites were selected to analyse the proposed method as seen in Figure 1. Site A was used to implement the DST method, while site B, which is located in the zone of 4°28′0″–4°28′8″ latitudes and 101°22′31″–101°22′44″ longitudes, was used for comparison with recent published technique. The considerations for selecting site B were taken to avoid the missing in number of classes.

3. Methodology

3.1. LiDAR data

The LiDAR point cloud was acquired over 26.7 km^2 of the Ringlet and surrounding area in Cameron Highland at a flying height of about 1510 m. The data was captured by using Riegl LM Q5600 scanner and Camera Hassleblad 39Mp on 15th of January 2015. The spatial resolution of camera was 13 cm, and the angles of laser scanner and camera were 60° and ±30°, respectively. The posting
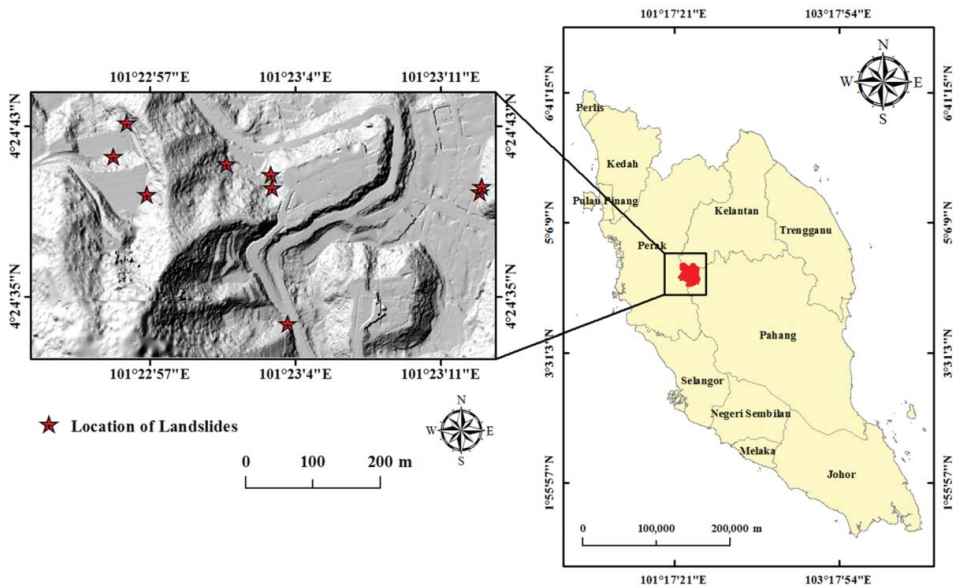
Figure 1. Study area and location of landslides.

density of the LiDAR data was 3–4 pts/m^2 (average point spacing = 0.41 m). The point density is closely spaced with 8 points per square metre with a 25,000 Hz pulse rate frequency. The absolute accuracy of the LiDAR data should meet the root mean square errors (RMSE) of 0.15 m in the vertical axis and 0.3 in the horizontal axis. LiDAR data processing showed that the total number of points acquired from the study area was ∼18 million. The minimum and maximum elevations are 32.4 and 92.52 m, respectively. The LiDAR data have seven returns, and most of the points were collected in the first return (∼78% of the total number of points). Orthophotos were also acquired by the same system for the study area to support landslide identification and characterization.

3.2. Landslide inventory

The landslide inventory produced previously by Pradhan and Lee (2010) was used to develop the proposed detection method and the total number of landslides is nine in the study with 286,970.54 m^2 as seen in Figure 1.

3.3. Data used and data processing

The filtering process is only performed to obtain a DTM or a DEM from a DSM. In addition, LiDAR data filtering is essential to analyse data and to reduce computational time. A DSM was generated by interpolating LiDAR point clouds using inverse distance weighting method (IDW) using the ArcGIS 10.3 software (Figure 2(a)). The DEM was constructed from the LiDAR point clouds at a 0.5-m spatial resolution using ArcGIS 10.3 software (Figure 2(b)). In the current study, multiscale curvature classification (MCC) is implemented for filtering the nonground points. It is a repeated algorithm for classifying LiDAR returns as ground and nonground (Evans and Hudak 2007). The algorithm integrates curvature filtering with a scale component and variable curvature tolerance. MCC interpolates a surface at various spatial resolutions through the thin-plate spline method, and points are classified based on a progressive curvature threshold parameter (Sameen et al. 2017). The value of this threshold was set to 0.77 via the trial-and-error method due to the topography of the study area.
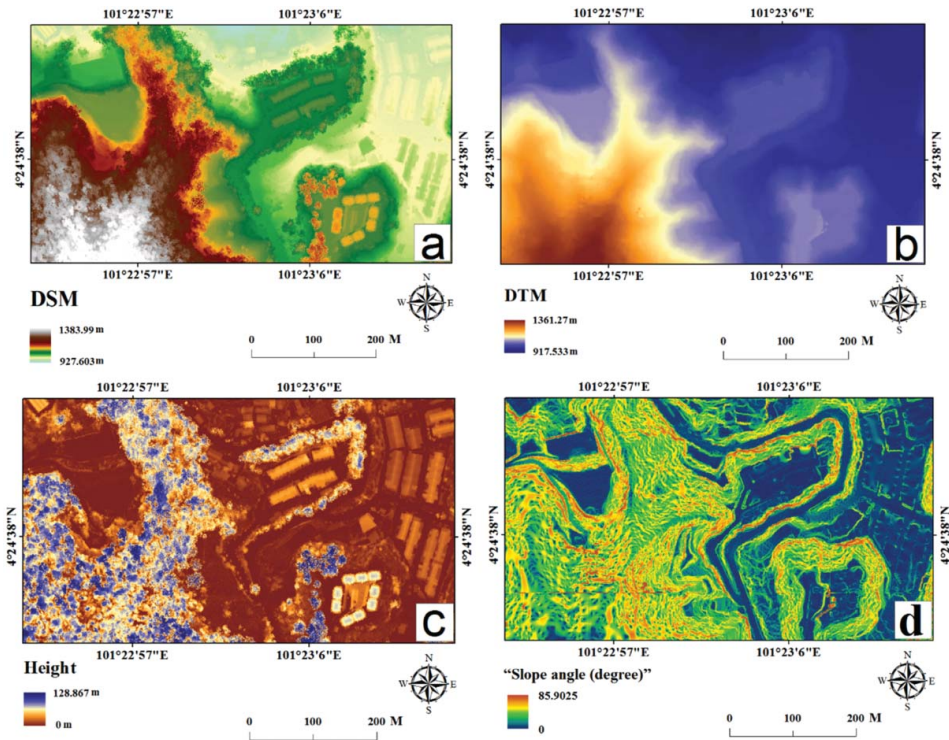
Figure 2. LiDAR-derived data: (a) DSM; (b) DTM; (c) height; and (d) slope angle.

Furthermore, a slope map (Figure 2(c)) was derived from the LiDAR DEM. These data were generated at 0.5-m spatial resolution with the spatial reference of GDM2000_Peninsula_RSO. Next, the height feature i.e. normalized DSM (nDSM) was derived by subtracting DSM from DEM (Figure 2(c)). These data provide extensive information on the landslide identification (Miner et al. 2010). Orthophoto image was registered on the same spatial reference of LiDAR point cloud using combined mutual information (Parmehr et al. 2014). Rectified orthophoto was used to produce Greenness Vegetation Index (Figure 3). The greenness was used to distinguish vegetation from non-vegetation areas and provide useful information. Greenness index was calculated using Equation (1) (Motohka et al. 2010):

$$\text{Greenness} = \frac{\text{Green} - \text{Red}}{\text{Green} + \text{Red}} . \tag{1}$$

3.4. Overall workflow

Figure 4 shows the overall workflow of automatic landslide detection using the DST method. This method requires several empirical parameters and uses two sets of data: LiDAR and orthophoto data. The first step in the workflow was generation of three sets of layers, greenness, height and slope, by processing both LiDAR and orthophoto data. After that, the DST fusion was applied through three steps: (1) finding the mass functions, (2) defining the support all mass functions, and (3) computing the plausibility. Two fused evaluations were conducted on site 'A' to detect the landslide location: (greenness and nDSM) and (greenness and slope) fusions. In the fusion process, empirical parameters were determined for landslide detection. Subsequently, the results of evolution
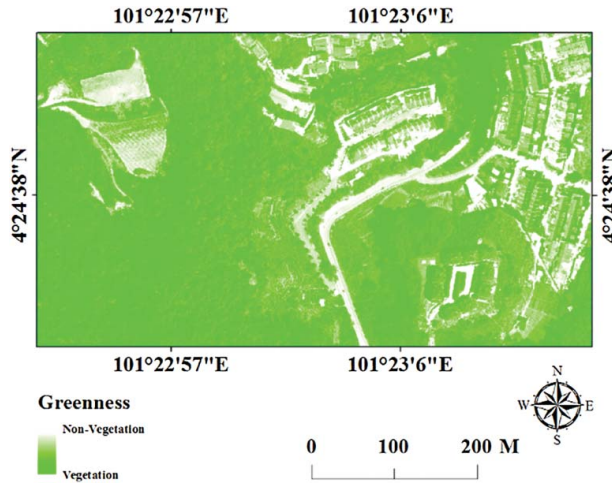
Figure 3. Greenness index derived from orthophotos.

fusion of DST fusion were assessed using two validation techniques: confusion matrix and area under the curve (Pradhan et al. 2016). The best evaluation fusion was compared with a recently published paper (Li et al. 2015). This comparison was based on RF algorithm using site 'B' to show the performance of the proposed method. Finally, the method was validated with the available landslide inventories.

3.5. Dempster–Shafer theory for fusion

DST mathematically integrates various data and calculates the associated evidential weight (Tangestani 2009). Derivation of DST from the Bayesian theory of probability has made this algorithm as a soft classifier (Wang et al. 2010). The detail about the DST can be seen in Rakowsky (2007). Handling the capability of incomplete data coverage supports the Dempster–Shafer approach (Feizizadeha et al. 2014). It is crucial to define the output result of belief, disbelief, plausibility and uncertainty precisely as stated by the DST concept (Althuwaynee et al. 2012). As per this theory, representation of the information requires a belief interval, along with mass functions. It is worth to note that higher flexibility for the specification of uncertainty in probabilistic models and hypothesis testing is afforded by the DST (Ducey 2001). There are three important functions in DST, namely, basic probability assignment function, belief function (*Bel*) and plausibility function (*Pls*) (Althuwaynee et al. 2012). There are three important functions in DST, namely, basic probability assignment function, belief function (*Bel*) and plausibility function (*Pls*) (Althuwaynee et al. 2012). Dempster's rule of combination provides a tool for combining numerous spatial data layers. The interval between belief and plausibility illustrates the uncertainty of the knowledge about the target proposition (Park 2011).

DST assumes that the image represents features that need to be categorized into different classes. For instance, if C1, C2, C3, $Cj \in \theta$, where θ is the set of hypotheses about a pixel class where the frame of discrimination is finite, i.e. 2^θ. In this work, four hypothetical classes, building (B), vegetation (V), cut slope (C) and landslide (L), are considered, $\theta = 4$. Meaning that the frame of discernment is $2^4 = 16$ classes, which signifies that either single classes (B, V, C and L), union of the classes (C ∪ V, B ∪ L, B ∪ V and C ∪ L) or one empty class.

From data sources, evidential weight (for a single or union of the classes) can be extracted and assigned to every pixel in the data sets. The DST algorithm is applied through three stages, such as finding mass function m (f) by applying Equation (2) to derive the probability in single or union of
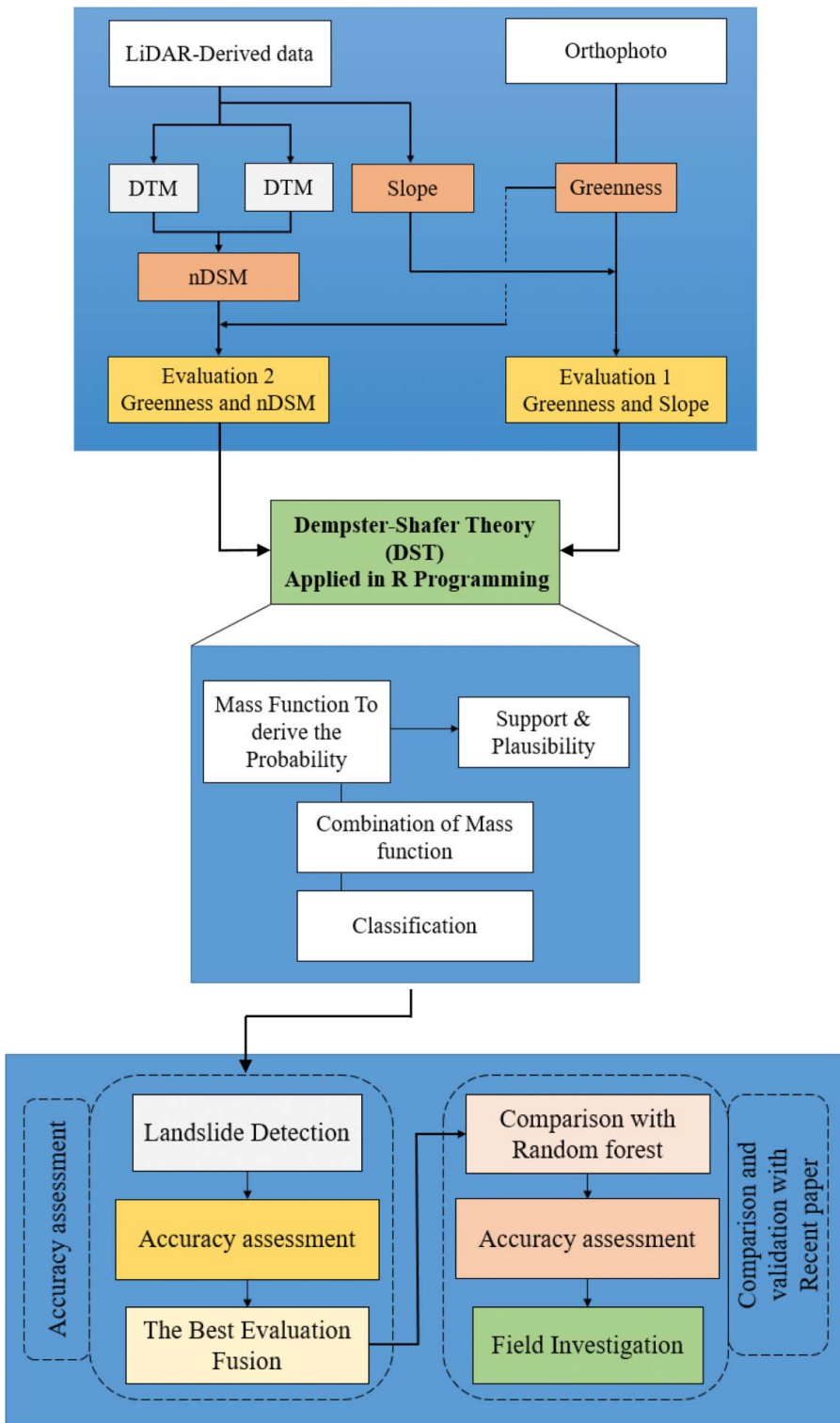
Figure 4. Detailed methodological flow chart used in this study.

classes using evidences from multisensory data independently (Saeidi et al. 2014).

$$m (\theta) = \begin{cases} 0 \leq m (\theta) \geq 1 \\ \sum_{c \in 2^\theta} m (C) = 1 \\ m (\emptyset) = 0 \end{cases} \qquad (2)$$

where $\emptyset$ interprets the empty class.

In the second step, for each class $C \in 2^\theta$, the sum of all mass functions that contribute evidences from data source is defined by Equation (3). Finding the plausibility over mass function for each class $C \in 2^\theta$, and defining the sum of all masses that do not have any contributing evidence to the proposed class is expressed in Equation (4) (Saeidi et al. 2014).

$$Sup(C) = \sum_{ci \in c} mC_i \qquad (3)$$

$$Pls = \sum_{ci \cap c \neq \emptyset} mC_i \qquad (4)$$

The support of each class defines its minimum uncertainty as seen in Figure 5. Plausibility represents maximum uncertainty of the class (Lu et al. 2006). Therefore, interval between $Sub (C)$ and $Pls (C)$ with $Sub (C) \leq Pls (C)$ can be defined by uncertainty. Eventually, the DST rule of combination allocates multiple mass functions into each single function from the whole contributors (Wang et al. 2010).

The combined probability mass functions for every four hypothetical classes are building (B), vegetation (V), cut slope (C) and landslide (L), which are found in Equation (5).

$$Combine (C) = \begin{cases} \dfrac{\sum_{c1 \cap c2 \cap \cdots cp} = c \prod_{1 \leq i \leq p} m(C_i)}{1 - k} \\ k = \sum_{c1 \cap c2 \cap \cdots cp = \emptyset} \prod_{1 \leq i \leq p} m(C_i) \end{cases} \qquad (5)$$

where k is the measure of conflict in the cues or multi-sensor data sets. As per rules of combination, the evidential probability for every pixel is combined with the super support class according to decision rule (Bellenger and Gatepaille 2011).

3.6. Definition of the probability masses

Apparent evidence for every class or union of the classes in every input data set is provided by the probability mass function. Several parameters and rules need to be defined before modelling the probability mass function (Rottensteiner et al. 2007). For easy implementation, we assumed
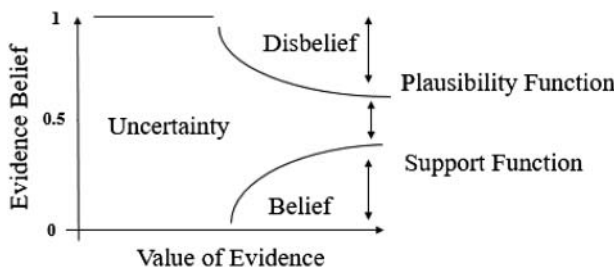

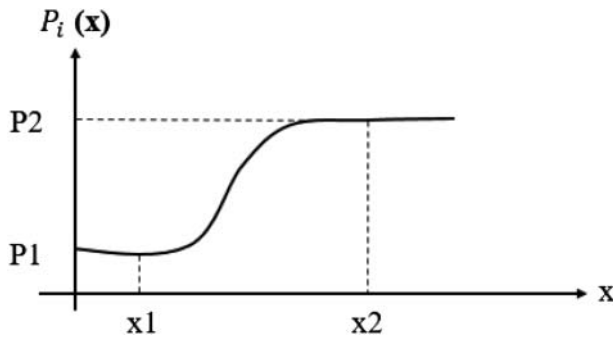Figure 5. Relation between support, plausibility and uncertainty.

Figure 6. Probability mass function modelling (PMF).

discrimination between C_1 and C_2 features in a data set, where $C_1, C_2 \in 2^\theta$, $C_1 \cap C_2 = \emptyset$, and $C_1 \cup C_2 = \theta$. After that, probability mass function was defined as $P_i(x)$ for every data set i and every pixel in the data set x_i using the parameters in Equation (6).

$$P_I(x) = \begin{cases} P_1 & \forall x \,|\, x \le x_1 \\ \begin{aligned} &P_1 + (P_2 - P_1) \\ &\times \left[3 \times \left(\frac{x_j - x_i}{x_2 - x_1} \right)^2 - 2 \times \left(\frac{x_j - x_i}{x_2 - x_1} \right)^3 \right] \end{aligned} & \forall x \,|\, (x_1 < x < x_2) \\ P_2 \,\forall x \,|\, x \le x_2 \end{cases}$$

(6)

where the probability masses $0 \le P_1 < P_2 \le 1$ for assigning each pixel x_j utilizing pre-identified threshold x_1 and x_2, whereas Figure 6 shows $x_1 < x_2$. For example, for data set, if the pixel value is greater than x_2, the probability mass P_2 will be assigned to the pixel. Hence, this will show the degree of pixel in class C_1.

3.6. Landslide detection based on Dempster–Shafer fusion

The DST of evidence is frequently applied to fuse data obtained from multiple sensors. Unlike Bayesian probabilistic reasoning, it offers tools to represent partial knowledge about sensor's contribution to the classification process. The research presented some general considerations with respect to the probability masses definition (Rottensteiner et al. 2005). Therefore, effective parameters are required for detecting the location of landslide; these parameters include greenness, height and slope, which are significant for automatic landslide detection (Liu et al. 2012). In addition, greenness, slope and height were crucial to identify landslide in remote sensing data (Chang et al. 2007, 2012; Rau et al. 2012; Pradhan et al. 2016). On the other hand, setting parameters and threshold could not clearly identify single classes, such as building and vegetation (Saeidi et al. 2014). Therefore, using empirical parameters, like greenness, nDSM and slope could be used to identify the classes. They were defined by applying minimum and maximum thresholds ×1 and ×2. For example, the probability P_1 coincides with input parameters that are lower than ×1; in this case, it is unlikely that the pixel is assigned to a hypothetical class. However, when the parameter is greater than ×2, high probability P_2 is assigned.

Figure 7 shows data set parameters (i.e. greenness, slope and height) defined based on iterative trial-and-error optimization method. The parameters (X_1, X_2, P_1 and P_2) were used to identify the location of landslide. In this study, the parameters of greenness set to $X_1 = 176$, $X_2 = 228$ were defined after several trials and errors, whereas, the probabilities of greenness were set to $P_1 = 0.2$ and
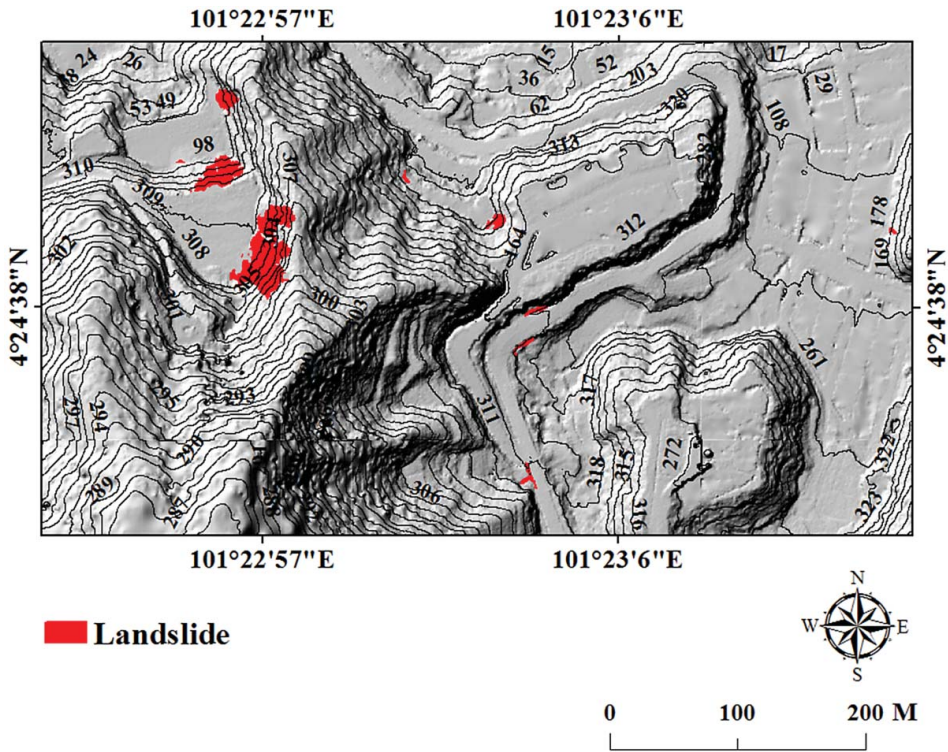
Figure 7. Results showing the location of landslides identified by fused (greenness and nDSM).

$P_2 = 0.8$ and were defined such that the visual interpretation of these thresholds provided 80% certainty, i.e. if the greenness of landslide is greater than 228, it could be either landslide or other class. Also, if the greenness of landslide is less than 176, the probability is that either another class or landslide is only 20%. Likewise, probabilities of slope were set to $X_1 = 20.3°$, $X_2 = 37.5°$, $P_1 = 0.05$ and $P_2 = 0.95$, whereas, height was set to $X_1 = 0.47$, $X_2 = 0.96$, $P_1 = 0.05$ and $P_2 = 0.95$ and were defined by the same method as presented in Table 2. Optimal thresholds are represented by red dots in the graph, whereas blue dots are other evaluated values. These thresholds were tested and compered on the test area. Results indicated that defined minimum and maximum thresholds were acceptable and accurate in dense vegetated area of various terrains.

Therefore, these parameters may help to identify landslide location in dense vegetation areas such as in Cameron Highlands, Malaysia. Table 1 shows the probability masses and also combined

Table 1. Evidential probability and combined probability masses from greenness and NSDM.

C_i class	nDSM	Greenness	Combined probability mass
Building	0	0	$\frac{P_{\Delta H} \times (1 - P_{Greenness})}{1 - K}$
Tree	0	0	$\frac{P_{\Delta H} \times P_{Greenness}}{1 - K}$
Other (Road + Soil + Grass)	0	0	$\frac{(1 - P_{\Delta H}) \times P_{Greenness}}{1 - K}$
Landslide	0	0	$\frac{(1 - P_{\Delta H}) \times (1 - P_{Greenness})}{1 - K}$
O ∪ T	0	$P_{Greenness}$	0
B ∪ L	0	$1 - P_{Greenness}$	0
B ∪ T	$P_{\Delta H}$	0	0
O ∪ L	$1 - P_{\Delta H}$	0	0

$1 - K = 1 - P_{\Delta H} \times (1 - P_{Greenness}) - (1 - P_{\Delta H}) \times P_{Greenness} - P_{\Delta H} \times P_{Greenness} - (1 - P_{\Delta H}) \times (1 - P_{Greenness}).$

Table 2. Defining parameters of each data for identifying landslide location.

Data	Empirical parameters				Identify features
	x_1	x_2	P_1	P_2	
Greenness	176	228	0.2	0.8	Landslide
Height	0.27	0.96	0.05	0.95	
Slope	$20.3°$	$37.5°$	0.05	0.95	

probability masses for greenness and nDSM fusion. Probability for fusion (greenness and slope) was assigned to be similar as that of the previous data set (greenness and nDSM).

Every cue (the research rather use the term 'cue', because some of the cues are derived from one sensor only) in R programming was used to calculate all the mass functions as well as the combined probability masses. Thereafter, the pixels were labelled by the maximum support to a class as expressed in Equation (7).

$$1 - K = 1 - P_{\Delta H} \times (1 - P_{Greenness}) - (1 - P_{\Delta H}) \times P_{Greenness} - P_{\Delta H} \times P_{Greenness} - (1 - P_{\Delta H}) \times (1 - P_{Greenness})$$

$$(7)$$

wherein $1 - K$ is the denominator in the normalization equation (5).

4. Results and discussion

In the current study, DST was applied to identify locations of landslide in vegetated areas. Empirical parameters (x_1, x_2, P_1 and P_2) were defined for identifying the class (i.e. landslide) (see Table 2). x_1, x_2 represent the minimum and maximum values in each set of data, respectively. For instance, greenness values were confined within a range of 21–511, whereas P_1 and P_2 represent the probability thresholds of the class value (i.e. how the pixel is assigned to a class by defining the thresholds). Landslide thresholds were determined visually by examining the respective data sets with respect to their statistical parameters.

4.1. Results of the fusions

DST was applied to fuse two sets of data: LiDAR-derived data and greenness index derived from orthophtos, and two evaluated fusions were applied. The results of the first evaluation fusion (Greenness and nDSM) are shown in Figure 8. The result showed that the qualitative assessment was reasonably accurate. However, some misclassification between landslide and cut-slope occurred because of the similarity in their pixel values in this part of the study area and the presence of two locations of unidentified landslide which appeared due to variations in the topographic areas. In this regard, it is worth to note that the landslide boundaries were not identified completely. Quantitative assessment showed that the overall accuracy and Kappa coefficient for landslide detection were 73% and 0.69, respectively. The results of the second evaluated fusion (Greenness and slop) are shown in Figure 9. The results showed an efficient, reliable and accurate detection of the landslide locations. The overall accuracy of fused greenness and slope was 82.33% and Kappa coefficient was 0.8. In addition, the results assessment for both first and second evaluations fusion based on the area under the curve method were 0.7 and 0.81, respectively. This indicates that slope factors are more appropriate than height due to several reasons; slope parameter can be calculated accurately because it requires only DEM. Meanwhile, height requires both digital surface and DEMs. Aggregating the outliers and noise in DSM and DTM led to increase the noise at landslide location compared to using only one data sources (for calculating slope feature), and height may not be measured accurately in vegetated areas (Rau et al. 2012). Thus, it can be said that DST gave good accuracy with high-resolution LiDAR data and orthophoto images. Furthermore, the high resolution of LiDAR-derived data and greenness derived from orthophoto image were effective and helped for identifying location of
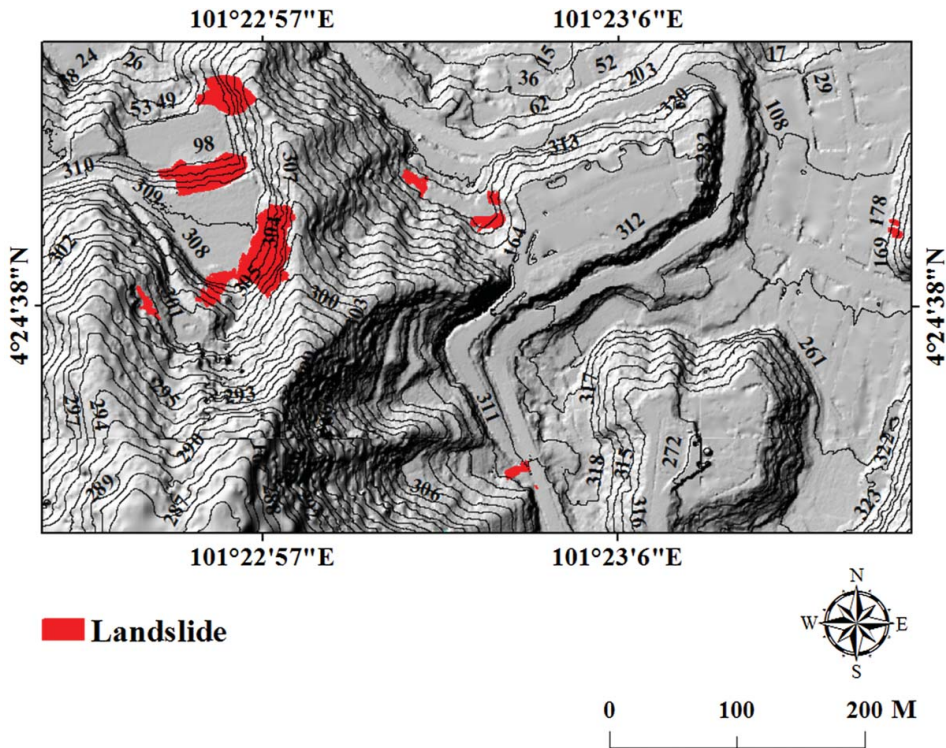
Figure 8. Results showing the location of landslides identified by fused (greenness and slope).

landslides. Consequently, the empirical parameters in DST provided a distinction between landslides and non-landslides. In addition, visual interpretation revealed that most of the landslides fall within the slope range of 20.3°–37.3°.

4.2. Comparison with random forest algorithm

The comparative study was done between the proposed method (greenness and slope) and the RF developed by Li et al. (2015). To apply the RF method in site B, all their method considerations were adopted. The segmentation result with a scale of 75 was selected. The scale segmentation was based on the trial-and-error method. Moreover, the training samples of landslides and non-landslides were roughly equal. The same input features selection was adopted and the same software was used throughout the study. The RF classifier was detected as three out of seven landslide locations over north-east, south and north-west of test area, as shown in Figure 10, whereas, DST detected all the landslide locations over the test area as seen in Figure 11. The validation results of the RF showed an overall accuracy of 73%; meanwhile, the proposed DST method achieved 77% as shown in Figure 12.

    It was difficult to compare the results of the proposed method with that of RF classifier due to various reasons, such as (1) the discrepancy in the data sets and types of the landslides, (2) limited training samples, (3) the difficulty of using all the significant features with one particular segmentation scale (Stumpf and Kerle 2011), and (4) the sudden changes in the topographic locations of the landslide effect on mean attributes that lead to low accuracy (Van Den Eeckhaut et al. 2012). Furthermore, supervised algorithms require prior knowledge of the study area, which is expensive and time-consuming (Le Hegarat-Mascle et al. 1997).
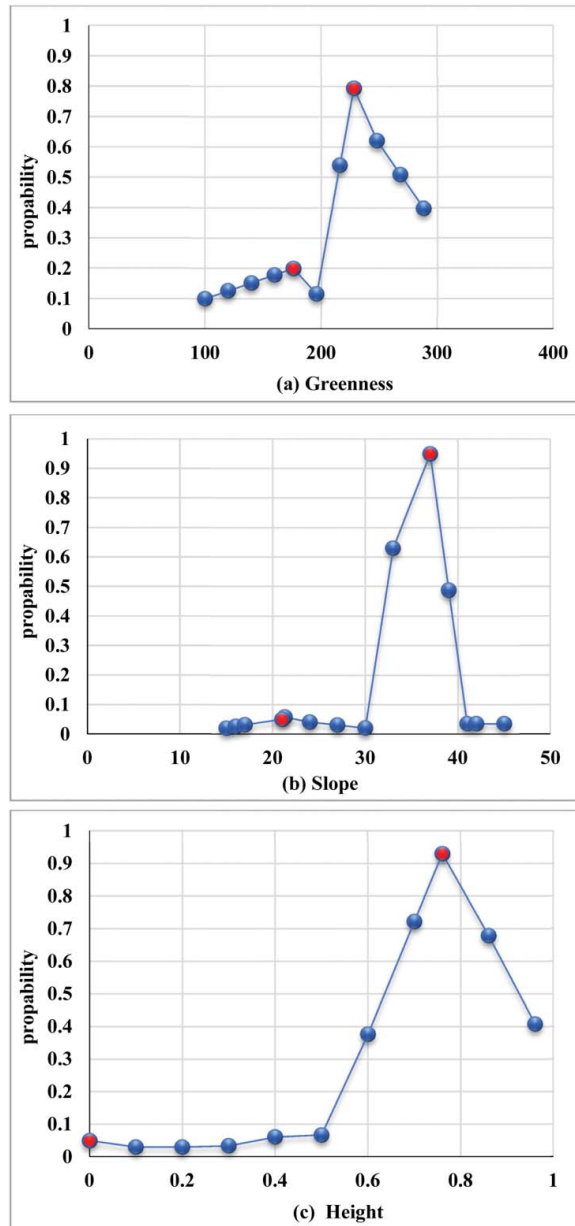
Figure 9. Evaluated values of (a) greenness, (b) slope and (c) height parameters by trial-and-error approach to determine the best thresholds for landslide detection.

In contrast, DST relies on logical reasoning with the evidence provided in the combined data sets to produce fast and accurate landslide map. The tendency of the scheme simultaneously fuses multiple data and performance classification without iterative programming procedure and is considered as one of the main advantages applied in this study. Therefore, more accurate classifier was generated by the probabilistic method (Liu et al. 2011) without requiring any manually selected training sites or data collection from the field. DST is time- and cost-effective unlike the supervised approach. Moreover, it does not require training data and prior knowledge about the study area (Le Hegarat-Mascle et al. 1997).
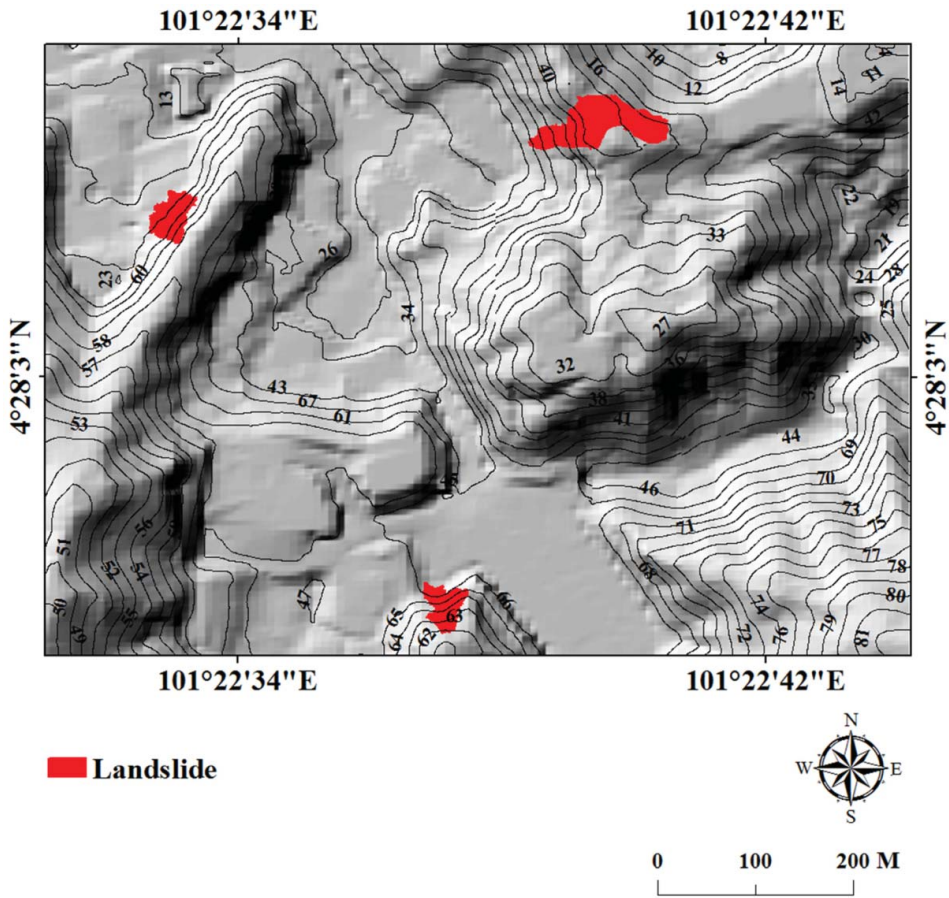
Figure 10. Results of random forest algorithm on the test area.

4.3. Accuracy assessment

Several techniques have been established for assessment of the accuracy of remote sensing products. In this research, accuracy assessment was examined based on confusion matrix (Sameen et al. 2017) and area under the curve (Feizizadeh et al. 2017) techniques to evaluate the effectiveness of the proposed method. The overall accuracies of the proposed methods and RF algorithm based on confusion matrix are shown in Tables 3 and 4, whereas, the receiver operating curves (ROC) of all the aforementioned methods are shown in Figures 10–14, respectively.

4.4. Field validation

The field investigation is considered as an additional assessment method to examine the reliability of the proposed method. A GeoExplorer 6000 handheld Global Positioning System (GPS) was used to identify the landslide locations during multiple field investigation (Figure 15). The used method for mapping the landslide inventory map was found to be precise and reliable as per the details obtained from the site measurement. Therefore, this suggests that the present methodology can be performed to identify the accurate locations of the landslides that resemble those obtained in the previous years.
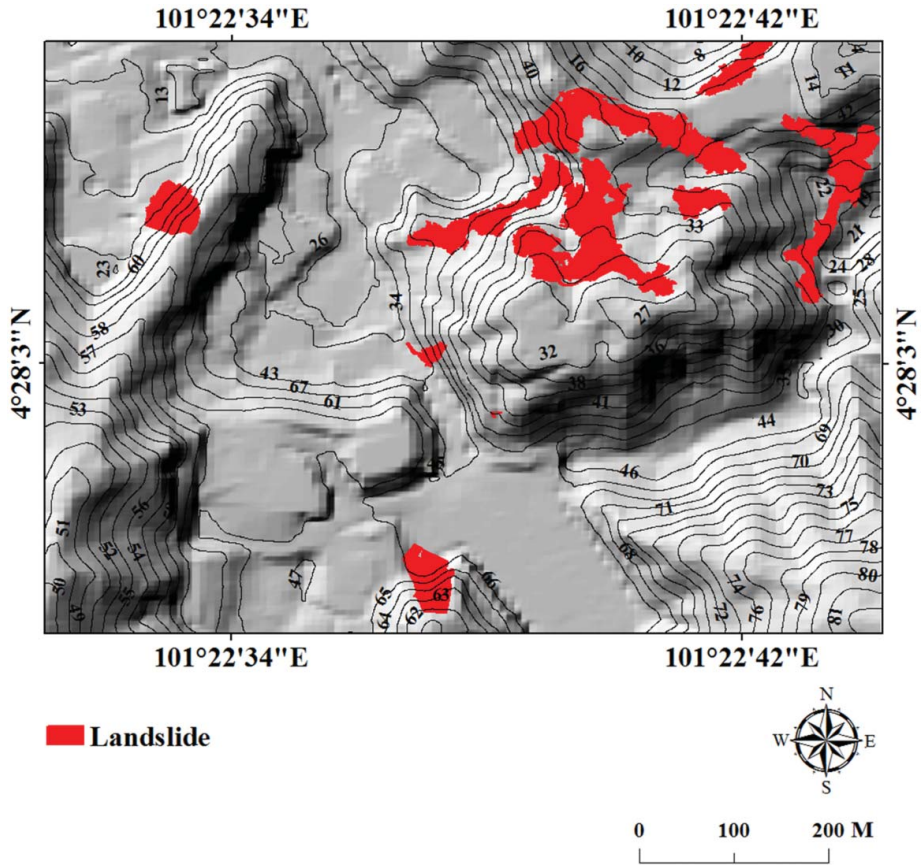
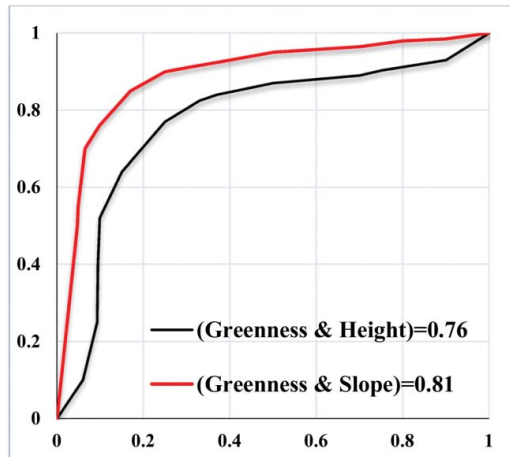Figure 11. Results of fusion (greenness and slope).

Figure 12. ROC curve for landslides detected in the study area.

Table 3. Result of accuracy assessment applied on the study area.

	Accuracy of detected landslides	
	Greenness–nDSM	Greenness–slope
Overall Acc.	73.4%	84.33%
Kappa coefficient	0.64	0.77

Table 4. Result of accuracy assessment applied on test area.

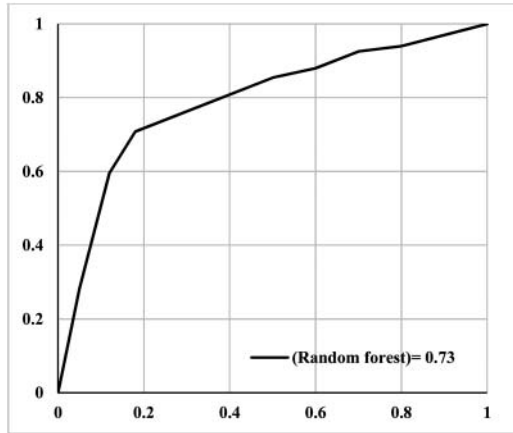|	Accuracy of detected landslides	
	Random forest	Greenness–slope
Overall Acc.	69.4%	79%
Kappa coefficient	0.62	0.73

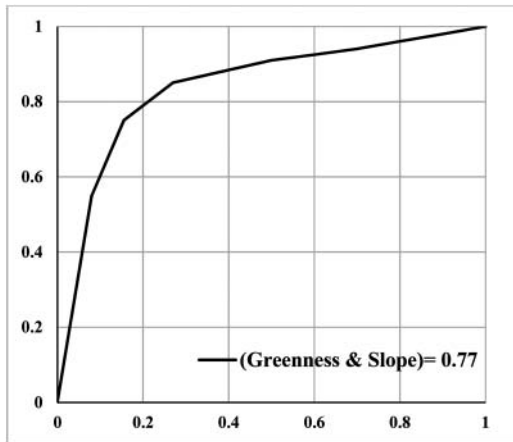Figure 13. ROC curve of supervised random forest on test area.

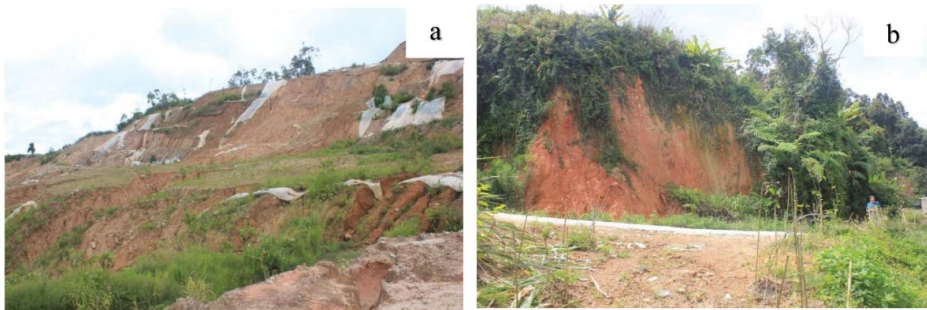Figure 14. ROC curve of greenness and slope on test area.

Figure 15. Field photographs showing landslides in (a) Taman Ringlet; and (b) Tanah Rata.

5. Conclusion

This study aimed to produce accurate landslide mapping with use of an efficient technique. DST was applied to fuse high-resolution LiDAR-derived products and greenness index generated from orthophoto imagery for identifying and mapping location of landslides. In tropical countries, such as Cameron Highlands in Malaysia, preparation of the landslide inventory is a challenging task because of the rapid growth of vegetation. Training data selection in the dense vegetated area is difficult and a time-consuming task making it crucial to use rapid and accurate techniques as well as effective parameters. Consequently, DST was applied to fuse high-resolution LiDAR-derived data products and greenness index derived from orthophoto images. The results were produced and validated using two validation approaches: confusion matrix and area under the curve. Accuracy assessment for fusion of greenness and nDSM provided a good accuracy to identify the landslide locations. Meanwhile, fusion of greenness and slope produced respectable and valuable details to identify the locations. This research demonstrated that the parameters derived from LiDAR data and orthophoto significantly enhanced the result's accuracy for identifying location of landslides. Defining the empirical parameters was significantly valuable for identifying location of landslides in dense vegetation. In addition, DST provided better accuracy when high-resolution LiDAR-derived data and orthophoto images were used.

Furthermore, the result of the proposed fusion method was compared with a recently published method based on RF algorithm. It shows that the overall accuracy of the RF algorithm and our proposed method were 73% and 77%, respectively. Results of the comparison study revealed that it was difficult to compare between those obtained by the proposed method and by the RF classifier due to the discrepancy in the data sets and types of the landslides, and limited training samples. In contrary, DST provided a unique characteristic that was impossible to get using other classification systems. Its uniqueness is attributed to its ability to independently investigate the degree of reliability using conflict, plausibility, uncertainty and support map on the information. This improves the precision in feature detection and makes the classification more reliable. Additionally, field data was used to perform the second round of validation. The outcomes showed that the location of landslides that were detected using the proposed method were actual and occurred in the past. Therefore, the success of the current research confirms the reliability of the proposed methodology to detect the landslide locations and produce a good inventory map.

Disclosure statement

ORCID

Biswajeet Pradhan http://orcid.org/0000-0001-9863-2054

References

Althuwaynee OF, Pradhan B, Lee S. 2012. Application of an evidential belief function model in landslide susceptibility mapping. Comput Geosci. 44:120–135. doi:10.1016/j.cageo.2012.03.003.

Althuwaynee OF, Pradhan B, Park HJ, Lee JH. 2014. A novel ensemble bivariate statistical evidential belief function with knowledge-based analytical hierarchy process and multivariate statistical logistic regression for landslide susceptibility mapping. Catena. 114:21–36.

Ardizzone F, Cardinali M, Galli M, Guzzetti F, Reichenbach P. 2007. Identification and mapping of recent rainfall-induced landslides using elevation data collected by airborne Lidar. Nat Hazards Earth Syst Sci. 7(6):637–650.

Bellenger A, Gatepaille S. 2011. Uncertainty in ontologies: Dempster–Shafer theory for data fusion applications. arXiv Preprint arXiv: 1106.3876.

Bui DT, Pradhan B, Lofman O, Revhaug I, Dick OB. 2012. Spatial prediction of landslide hazards in Hoa Binh province (Vietnam): a comparative assessment of the efficacy of evidential belief functions and fuzzy logic models. Catena. 96:28–40.

Carranza E, Hale M, Faassen C. 2008. Selection of coherent deposit-type locations and their application in data-driven mineral prospectivity mapping. Ore Geol Rev. 33(3):536–558.

Chang KT, Chiang SH, Hsu ML. 2007. Modeling typhoon-and earthquake-induced landslides in a mountainous watershed using logistic regression. Geomorphology. 89(3):335–347.

Chang KT, Liu JK, Wang CI. 2012. An object-oriented analysis for characterizing the rainfall-induced shallow landslide. J Mar Sci Technol. 20(6):647–656.

Chen W, Li X, Wang Y, Chen G, Liu S. 2014. Forested landslide detection using LiDAR data and the random forest algorithm: a case study of the Three Gorges, China. Remote Sens Environ. 152:291–201.

Chu H, Zhu W. 2008. Fusion of IKONOS satellite imagery using IHS transform and local variation. IEEE Geosci Remote Sens Lett. 5(4):653–657.

Demir N, Poli D, Baltsavias E. 2009. Detection of buildings at airport sites using images & LiDAR data and a combination of various methods. Paper presented at: Proceedings of ISPRS Workshop CMRT09 on Object Extraction for 3D City Models, Road Databases and Traffic Monitoring—Concepts, Algorithms and Evaluation; Paris, France.

Ducey MJ. 2001. Representing uncertainty in silvicultural decisions: an application of the Dempster–Shafer theory of evidence. For Ecol Manage. 150(3):199–211.

Elghazali E. 2011. Performance of quickbird image and Lidar data fusion for 2D/3D city mapping. Austral J Basic Appl Sci. 7(11):1588–1600.

Evans JS, Hudak AT. 2007. A multiscale curvature algorithm for classifying discrete return LiDAR in forested environments. I IEEE Trans Geosci Remote Sens. 45(4):1029–1038.

Feizizadeh B, Blaschke T. 2013. GIS-multicriteria decision analysis for landslide susceptibility mapping: comparing three methods for the Urmia lake basin. Iran Nat Hazards. 65(3):2105–2128.

Feizizadeh B, Blaschke T, Nazmfar H. 2014. GIS-based ordered weighted averaging and Dempster–Shafer methods for landslide susceptibility mapping in the Urmia Lake Basin, Iran. Int J Digit Earth. 7(8):688–708.

Feizizadeh B, Jankowski P, Blaschke T. 2014. A GIS based spatially-explicit sensitivity and uncertainty analysis approach for multi-criteria decision analysis. Comput Geosci. 64:81–95.

Feizizadeh B, Roodposhti MS, Blaschke T, Aryal J. 2017. Comparing GIS-based support vector machine kernel functions for landslide susceptibility mapping. Arab J Geosci. 10(5):122.

Galli M, Ardizzone F, Cardinali M, Guzzetti F, Reichenbach P. 2008. Comparing landslide inventory maps. Geomorphology. 94(3):268–289.

Gibril MBA, Bakar SA, Yao K, Idrees MO, Pradhan B. 2016. Fusion of RADARSAT-2 and multispecral optical remote sensing data for LULC extraction in a tropical agricultural area. Geocarto Int. 32(7):735–748.

González-Audicana M, Saleta JL, Catalán RG, García R. 2004. Fusion of multispectral and panchromatic images using improved IHS and PCA mergers based on wavelet decomposition. IEEE Trans Geosci Remote Sens. 42(6):1291–1299.

Guzzetti F, Mondini AC, Cardinali M, Fiorucci F, Santangelo M, Chang KT. 2012. Landslide inventory maps: new tools for an old problem. Earth-Sci Rev. 112(1):42–66.

Guzzetti F, Reichenbach P, Csardinali M, Galli M, Ardizzone F. 2005. Probabilistic landslide hazard assessment at the basin scale. Geomorphology. 72 (1):272–299.

Hall DL, Llinas J. 1997. An introduction to multisensor data fusion. Proc IEEE. 85(1):6–23.

Hnatushenko V, Vasyliev V. 2016. Remote sensing image fusion using ICA and optimized wavelet transform. ISPRS J Photogramm Remote Sens. XLI-B7:653–659.

Jebur MN, Pradhan B, Tehrany MS. 2014. Detection of vertical slope movement in highly vegetated tropical area of Gunung pass landslide, Malaysia, using L-band InSAR technique. Geosci J. 18(1):61–68.

Jiang D, Zhuang D, Fu J, Huang Y. 2011. Survey of multispectral image fusion techniques in remote sensing applications. China: INTECH Open Access Publisher; p. 1–22.

Kabolizade M, Ebadi H, Ahmadi S. 2010. An improved snake model for automatic extraction of buildings from urban aerial images and LiDAR data. Comput Environ Urban Syst. 34(5):435–441.

Kaur ER, Sharma EM, Kaur EA. 2016. Image fusion and its various techniques: a review. Image. 4(1):59–62.

Le Hegarat-Mascle S, Bloch I, Vidal-Madjar D. 1997. Application of Dempster–Shafer evidence theory to unsupervised classification in multisource remote sensing. IEEE Trans Geosci Remote Sens. 35(4):1018–1031.

Li X, Cheng X, Chen W, Chen G, Liu S. 2015. Identification of forested landslides using LiDar data, object-based image analysis, and machine learning algorithms. Remote Sens. 7(8):9705–9726.

Liu JK, Hsiao KH, Shih PTY. 2012. A geomorphological model for landslide detection using airborne LIDAR data. J Mar Sci Technol. 20(6):629–638.

Liu Y, Zhang HH, Wu Y. 2011. Hard or soft classification? Large-margin unified machines. J Am Stat Assoc. 106 (493):166–177.

Lu YH, Trinder JC, Kubik K. 2006. Automatic building detection using the Dempster–Shafer algorithm. Photogramm Eng Remote Sens. 72(4):395–403.

Malamud BD, Turcotte DL, Guzzetti F, Reichenbach P. 2004. Landslide inventories and their statistical properties. Earth Surf Proc Land. 29(6):687–711.

McKean J, Roering J. 2004. Objective landslide detection and surface morphology mapping using high-resolution airborne laser altimetry. Geomorphology. 57(3):331–351.

Mezaal MR, Pradhan B, Sameen MI, Mohd Shafri HZ, Yusoff ZM. 2017. Optimized neural architecture for automatic landslide detection from high−resolution airborne laser scanning data. Appl Sci. 7(7):730.

Miller PE, Mills JP, Barr SL, Birkinshaw SJ, Hardy AJ, Parkin G, Hall SJ. 2012. A remote sensing approach for landslide hazard assessment on engineered slopes. Trans Geosci Remote Sens. 50(4):1048–1056.

Miner A, Flentje P, Mazengarb C, Windle D. 2010. Landslide recognition using LiDAR derived digital elevation models-lessons learnt from selected Australian examples. In Proceedings of 11th IAEG Congress of the International Association of Engineering Geology and the Environment; Sep 5–10; Auckland, New Zealand. p. 5–9.

Mohammady M, Pourghasemi HR, Pradhan B. 2012. Landslide susceptibility mapping at Golestan province, Iran: a comparison between frequency ratio, Dempster–Shafer, and weights-of-evidence models. J Asian Earth Sci. 61:221–236.

Motohka T, Nasahara KN, Oguma H, Tsuchida S. 2010. Applicability of green–red vegetation index for remote sensing of vegetation phenology. Remote Sens. 2(10):2369–2387.

Nampak H, Pradhan B, Manap MA. 2014. Application of GIS based data driven evidential belief function model to predict groundwater potential zonation. J Hydrol. 513:283–300.

Neshat A, Pradhan B. 2015. Risk assessment of groundwater pollution with a new methodological framework: application of Dempster–Shafer theory and GIS. Nat Hazards. 78(3):1565–1585.

Parker RN, Densmore AL, Rosser NJ, De Michele M, Li Y, Huang R, Petley DN. 2011. Mass wasting triggered by the 2008 Wenchuan earthquake is greater than orogenic growth. Nat Geosci. 4(7):449–452.

Parmehr EG, Fraser CS, Zhang C, Leach J. 2014. Automatic registration of optical imagery with 3D LiDAR data using statistical similarity. ISPRS J Photogramm Remote Sens. 88:28–40.

Pradhan B, Abokharima MH, Jebur MN, Tehrany MS. 2014. Land subsidence susceptibility mapping at Kinta Valley (Malaysia) using the evidential belief function model in GIS. Nat Hazards. 73(2):1019–1042.

Pradhan B, Jebur MN, Shafri HZM, Tehrany MS. 2016. Data fusion technique using wavelet transform and Taguchi methods for automatic landslide detection from airborne laser scanning data and quickbird satellite imagery. IEEE Trans Geosci Remote Sens. 54(3):1610–1622.

Pradhan B, Lee S. 2010. Regional landslide susceptibility analysis using back-propagation neural network model at Cameron Highland, Malaysia. Landslides. 7(1):13–30.

Pradhan B, Mezaal MR. 2017. Optimized rule sets for automatic landslide characteristic detection in a highly vegetated forests. In: Pradhan B, editors. Laser scanning applications in landslide assessment. Cham: Springer. https://doi.org/10.1007/978-3-319-55342-9_3

Rakowsky UK. 2007. Fundamentals of the Dempster–Shafer theory and its applications to reliability modeling. Int J Reliab Qual Saf Eng. 14(06):579–601.

Rau JY, Chang KT, Shao YC, Lau CC. 2012. Semi-automatic shallow landslide detection by the integration of airborne imagery and laser scanning data. Nat Hazards. 61(2):469–480.

Rottensteiner F, Trinder J, Clode S, Kubik K. 2005. Using the Dempster–Shafer method for the fusion of LIDAR data and multi-spectral images for building detection. Inf Fusion. 6(4):283–300.

Rottensteiner F, Trinder J, Clode S, Kubik K. 2007. Building detection by fusion of airborne laser scanner data and multi-spectral images: performance evaluation and sensitivity analysis. ISPRS J Photogramm Remote Sens. 62 (2):135–149.

Saeidi V, Pradhan B, Idrees MO, Latif ZA. 2014. Fusion of airborne LiDAR with multispectral SPOT 5 image for enhancement of feature extraction using Dempster–Shafer theory. IEEE Trans Geosci Remote Sens. 52(10):6017–6025.

Sameen MI, Pradhan B, Shafri HZ, Mezaal MR, bin Hamid H. 2017. Integration of ant colony optimization and object-based analysis for LiDAR data classification. IEEE J-STARS. 10(5):2055–2066.

Stumpf A, Kerle N. 2011. Object-oriented mapping of landslides using random forests. Remote Sens Environ. 115 (10):2564–2577.

Tangestani MH. 2009. A comparative study of Dempster–Shafer and fuzzy models for landslide susceptibility mapping using a GIS: an experience from Zagros Mountains, SW Iran. J Asian Earth Sci. 35(1):66–73.

Tehrany MS, Pradhan B, Jebur MN. 2014. Flood susceptibility mapping using a novel ensemble weights-of-evidence and support vector machine models in GIS. J Hydrol. 512:332–343.

Tu TM, Huang PS, Hung CL, Chang CP. 2004. A fast intensity-hue-saturation fusion technique with spectral adjustment for IKONOS imagery. IEEE Geosci Remote Sens Lett. 1(4):309–312.

Vaiopoulos A, Karantzalos K. 2016. Pansharpening on the narrow Vnir and SWIR spectral bands of SENTINEL-2-ISPRS. J Photogramm Remote Sens. 41:723–730.

Van Den Eeckhaut M, Kerle N, Poesen J, Hervás J. 2012. Object-oriented identification of forested landslides with derivatives of single pulse LiDAR data. Geomorphology. 173:30–42.

Van Westen CJ, Castellanos E, Kuriakose SL. 2008. Spatial data for landslide susceptibility, hazard, and vulnerability assessment: an overview. Eng Geol. 102(3):112–131.

Vu TT, Yamazaki F, Matsuoka M. 2009. Multi-scale solution for building extraction from LiDAR and image data. Int J Appl Earth Obs. 11(4):281–289.

Wang H, Liu J, Augusto JC. 2010. Mass function derivation and combination in multivariate data spaces. Inf Sci. 180(6):813–819.

Wills C, McCrink T. 2002. Comparing landslide inventories: the map depends on the method. Environ Eng Geosci. 8(4):279–293.

Yu K, Hu N, Geng X, Zhao Y, Tang H. 2011. A new fusion algorithm for optical remote sensing data. In Image and Data Fusion (ISIDF), 2011 International Symposium on, Tengchong, Yunnan, China. IEEE. p. 1–4.

Zhang Z, Blum RS. 1997. Region-based image fusion scheme for concealed weapon detection. In Proceedngs of the 31st Annual Conference Information Sciences and Systems, Baltimore, MD. p. 168–173.